ADVANCED ENERGY MATERIALS
www.advenergymat.de

Highly Dispersed Cobalt Clusters in Nitrogen-Doped Porous Carbon Enable Multiple Effects for High-Performance Li–S Battery

Rui Wang, Jinlong Yang, Xin Chen, Yan Zhao, Wenguang Zhao, Guoyu Qian, Shunning Li, Yinguo Xiao,* Hao Chen, Yusheng Ye, Guangmin Zhou, and Feng Pan**

The lithium–sulfur (Li–S) battery is considered a promising candidate for the next generation of energy storage system due to its high specific energy density and low cost of raw materials. However, the practical application of Li–S batteries is severely limited by several weaknesses such as the shuttle effect of polysulfides and the insulation of the electrochemical products of sulfur and Li_2S/Li_2S_2. Here, by doping nitrogen and integrating highly dispersed cobalt catalysts, a porous carbon nanocage derived from glucose adsorbed metal–organic framework is developed as the host for a sulfur cathode. This host structure combines the reported positive effects, including high conductivity, high sulfur loading, effective stress release, fast lithium-ion kinetics, fast interface charge transport, fast redox of Li_2S_n, and strong physical/chemical absorption, achieving a long cycle life (86% of capacity retention at 1C within 500 cycles) and high rate performance (600 mAh g^{-1} at 5C) for a Li–S battery. By combining experiments and density functional theoretical calculations, it is demonstrated that the well-dispersed cobalt clusters play an important role in greatly improving the diffusion dynamics of lithium, and enhance the absorption and conversion capability of polysulfides in the host structure.

1. Introduction

Lithium batteries are key energy storage devices to meet the large-scale utilization of clean energy and electrical vehicles.[1,2] Among them, Li–S batteries with multi-electron reaction have attracted more attention due to their ultrahigh theoretical energy density (2600 Wh kg^{-1}).[3–6] However, a series of problems restrict the practical application of Li–S batteries, such as poor conductivity[7] and large volume change[8] between Li_2S (discharge) and S (charge) conversion, fast capacity decay due to polysulfides (Li_2S_n, $3 \le n \le 8$) shuttle between cathode and anode in liquid electrolyte,[9–11] and so on.

To solve above-mentioned problems and improve the cycle performance, it is of great significant to design and fabricate excellent sulfur hosts for lithium–sulfur batteries. Summarizing the previous literatures,[12–17] a good sulfur host structure should possess the following essential characteristics: 1) achieving high electronic conductivity to reduce the polarization resistance of sulfur cathode by mixing with advanced carbon materials (graphene, carbon nanotubes, and porous carbon)[18–20] or/and conductive polymers.[21] 2) Large specific surface area to realize high sulfur loading and provide more electric contact sites. 3) Nanostructure to shorten the migration distance of internal lithium ion. 4) Porous structure to absorb liquid Li_2S_n ($3 \le n \le 8$) and prevent their shuttle effect. According to these characteristics, many interesting structures have been reported as sulfur host to boost the lithium–sulfur batteries performance, such as multichannel carbon nanofibers[12] and CMK-3.[14] However, even using such highly conductive structure, lithium–sulfur batteries still suffer from quick decay, which results in poor cycle performance.

Recently, some novel chemical strategies, including strong chemical adsorption,[16,22] polarity miscibility,[23] and catalysis redox,[24–26] have been adopted in Li–S batteries to block the shuttle effect and accelerate the conversion of sulfur species. For example, many reports[22–28] show that there was significant chemical adsorption between pyridinic/pyrrolic nitrogen and liquid Li_2S_n, thus blocking liquid intermediates around the nitrogen during charge/discharge and enhancing the polarity of the carbon-based materials, resulting in greater contact with polar polysulfides, thereby enhancing interfacial charge transfer. In addition, many transition metals and their compounds,

R. Wang, Dr. J. Yang, X. Chen, Dr. Y. Zhao, W. Zhao, Dr. G. Qian, Dr. S. Li, Prof. Y. Xiao, Prof. F. Pan
School of Advanced Materials
Peking University
Shenzhen Graduate School
Shenzhen 518055, P. R. China
E-mail: yangjl@pkusz.edu.cn; y.xiao@pku.edu.cn; panfeng@pkusz.edu.cn
Dr. J. Yang, Dr. H. Chen, Dr. Y. Ye
Department of Materials Science and Engineering
Stanford University
Stanford, CA 94305, USA
Prof. G. Zhou
Tsinghua-Berkeley Shenzhen Institute
Tsinghua University
Shenzhen 518055, China
The ORCID identification number(s) for the author(s) of this article can be found under https://doi.org/10.1002/aenm.201903550.

DOI: 10.1002/aenm.201903550

such as oxides (Co_3O_4,[29] Fe_2O_3[30]), sulfides (ZnS,[31] VS_2,[32] CoS_2,[33] TiS_2[34]), nitrides/phosphides (TiN,[35] CoP[36]), also show strong chemical adsorption to Li_2S_n. Meanwhile, they also play important roles as catalysts to accelerate the kinetic reaction process of Li ions and polysulfides, improving high-rate capacity and stability of Li–S batteries.[34] Therefore, if we can take all these advantages and integrate multiple functions in single sulfur host, including high conductivity, high sulfur loading, effective stress release, fast lithium-ion kinetics, fast interface charge transport, fast redox of Li_2S_n, and strong (physical/chemical) absorption, it would be very promising to achieve high-performance lithium–sulfur cathode.

Metal–organic frameworks (MOF) and their derivatives are considered as excellent candidates for designing host structures with multiple effects due to their large Brunauer–Emmett–Teller (BET) area, abundant pore structure, easily controlled size and morphology, feasible element doping, and so on. For example, Zhou et al.[37] first used a variety of MOF (MIL-53 (Al), NH2-MIL-53 (Al), HKUST-1, ZIF-8) as host materials thereby obtaining long-cycle Li–S batteries. However, the long battery life was obtained only at a low sulfur content (30 wt%) because of the special pore structure and electrical conductivity. Thus, more studies[23,38–40] have focused on applying multifunctional pyrolytic carbon materials derived from MOF as host structures for Li–S batteries. For instance, Li et al.[38] reported that a new type of ZIF67-derived sulfur host containing cobalt and N-doped graphitic carbon exhibited an outstanding high rate response of up to 5C. However, cobalt nanoparticles in the host are very easy to agglomerate, which can only provide limiting reaction active sites.

Herein, we firstly used MOF to adsorb glucose and then carbonated to obtain a nitrogen-doped porous carbon (N-PC) nanocage with uniformly dispersed cobalt catalysts. The host structure derived from MOF enables high performance of Li–S battery with long cycle life (86% of the capacity retention within 500 cycles) and high rate performance (600 mAh g^{-1} at a high current density of 7.5 A g^{-1}). The high performance of this Li–S battery is mainly attributed to the multiple effect of the host structure on the intermediate of polysulfides (Li_2S_n) during charge and discharge. Combining with experiments and density functional theory (DFT) calculations, we demonstrated that the well-dispersed cobalt clusters greatly improved the diffusion dynamics of lithium and the enhanced absorption of polysulfides in the host structure.

2. Results and Discussions

The schematic diagram of synthesis route for sulfur cathode with multiple-effect host structure is shown in **Figure 1**a. First, as-prepared ZnCo-ZIF (synthesis method and structural characterization are shown in Figures S1 and S2 in the Supporting Information) was soaked into glucose solution. Glucose with

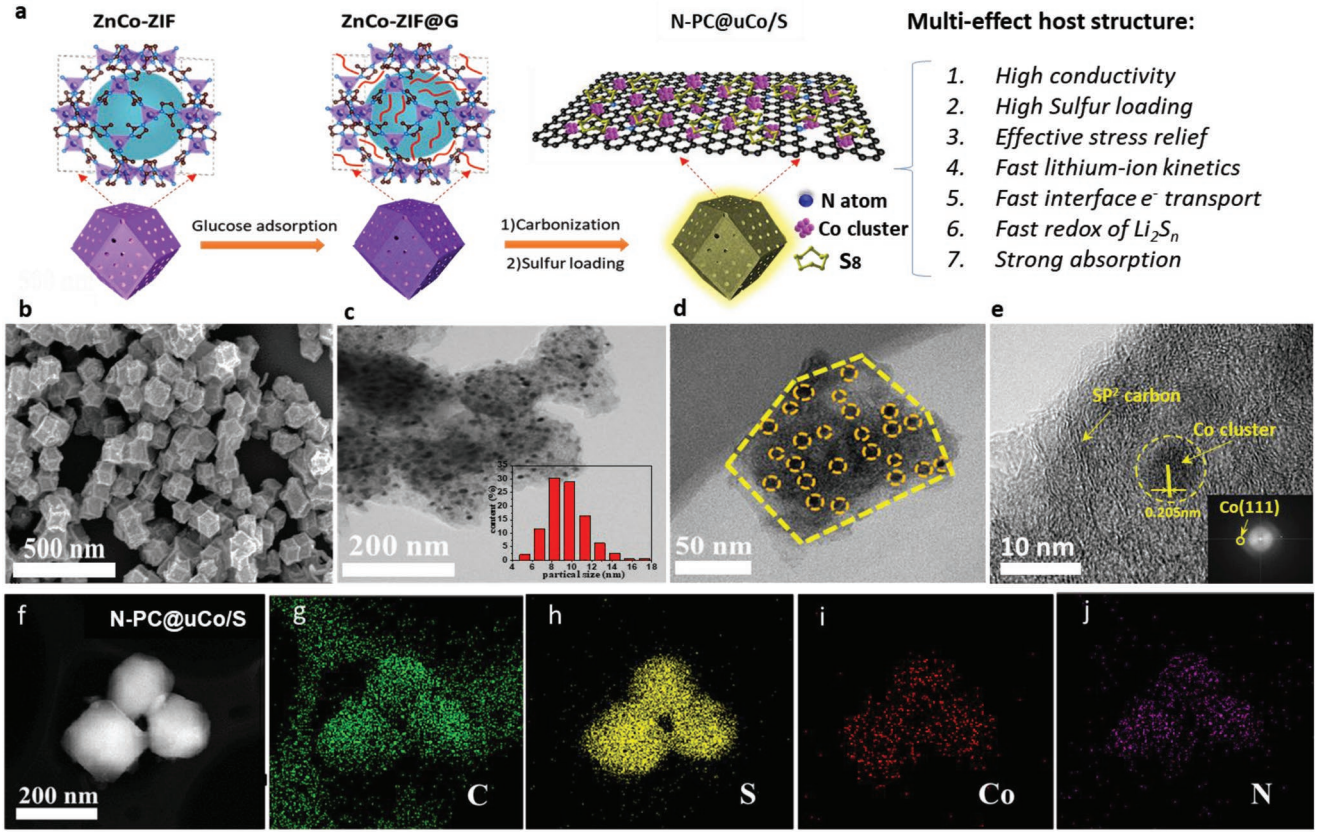

Figure 1. a) Schematic diagram of synthesis route for N-PC@uCo/S cathode with multiple effects. b) SEM, c,d) TEM, e) HR-TEM, f) HAADF-STEM images, and the corresponding g) C, h) S, i) Co, and j) N elemental mapping of N-PC@uCo/S. Inset of (c) is the distribution of Co cluster, inset of (e) is the corresponding FFT diffraction pattern.

molecule size <0.6 nm can be absorbed into the ZnCo-ZIF structure and formed a composite (ZnCo-ZIF@G) thanks to suitable pore size (1–2 nm) of ZnCo-ZIF (Figure S3, Supporting Information). Then, the nitrogen-doped porous carbon with uniformly dispersed cobalt clusters (N-PC@uCo) was obtained after the carbonization of ZnCo-ZIF@G. The obtained matrix was used as host structure by thoroughly mixing with sulfur powder (76 wt% of sulfur content, the detailed descriptions of experiments are given in the Supporting Information) to get a sulfur cathode material (N-PC@uCo/S), as shown in Figure 1a.

For comparison, the other two host structures, i.e., ZnCo-ZIF without Co source and without glucose, were also synthesized, respectively. Observing from scanning electron microscopy (SEM) images (Figure 1b and Figure S4, Supporting Information), the octahedral morphologies of ZIF were well maintained for all three samples after carbonization. However, transmission electron microscopy (TEM) images (Figure 1c–e and Figures S5 and S6, Supporting Information) demonstrate that the microstructure of these three samples is very different. For the host structure without Co source, Zn atoms are volatilized and only nitrogen-doped porous carbon framework remains, while in the sample without glucose, the cobalt nanoparticles with average size of ≈15 nm are segregated in the center of N-PC framework because cobalt source are molten and local agglomeration is gradually formed at high temperature. Consequently, the host structure is found to be a nitrogen-doped porous carbon with aggregated cobalt particles (N-PC@aCo). As shown in Figure 1c, in the host structure with glucose, many cobalt clusters with average size of 8–10 nm are uniformly dispersed in whole N-PC. The Co content in N-PC@uCo composite is ≈6.09 wt% by using weighting method and SEM–energy dispersive X-ray spectroscopy (EDS) analysis (Figure S7, Supporting Information). Thermogravimetric analysis (TGA, Figure S8, Supporting Information) shows that glucose is first carbonized at 410 °C to form a stable carbon structure inside ZnCo-ZIF, which will further form a stable graphitized sp^2 carbon structure (Figure 1d) at higher temperature, thus preventing the aggregation of cobalt and increasing dispersion during the decomposition of ZnCo-ZIF at $T > 600$ °C. Combining high-resolution transmission electron microscopy (HR-TEM) image with fast Fourier transform (FFT) diffraction pattern (Figure 1d) and X-ray diffraction (XRD) (Figure S9, Supporting Information), we further confirmed the existence of sp^2 carbon and metallic Co cluster in the N-PC@uCo composite. Therefore, we conclude that the fabrication of various host structure is successful as designed, and the dispersity and size of Co cluster can be effectively controlled in the synthesis process by adding glucose.

The sulfurization of three cathodes was realized by melting sulfur with the three-host structures. It can be observed from SEM images (Figures S10 and S11, Supporting Information), the original morphology can be maintained without agglomeration after loading sulfur, indicating that the sulfur has been effectively adsorbed to the inside of host structures. Furthermore, high-angle annular dark-field scanning transmission electron microscopy (HAADF-STEM) and the corresponding EDS mapping were used to identify the microstructure of these sulfur cathodes. The HAADF-STEM images of N-PC@uCo/S and N-PC@aCo/S (Figure 1f and Figure S12, Supporting Information) further illustrate the regular nanostructure of the composite. The elemental maps of C, S, Co, and N in N-PC@uCo/S composite clearly demonstrate that the elements are homogeneously distributed in the framework of N-PC. In particular, the signal of Co for N-PC@uCo/S cathode is more uniform than that in N-PC@aCo/S cathode, which is consistent with our design.

In order to identify the multiple effects of the host materials, detailed features of host and sulfur cathode structures are explored further by a series of characterizations. As shown in **Figure 2**a, nitrogen adsorption/desorption isotherms of three host structures show the joint of type I and IV isotherms, indicating the presence of both micropores and mesopores. Figure 2b shows that N-PC@uCo host has largest the pore volume of 0.98 $cm^3\ g^{-1}$ among the samples, which are attributed to the appearance of mesopores with size between 10 and 50 nm and micropores with an average size of 1.5 nm. Meanwhile, BET specific surface area of N-PC@uCo is deduced to be 1185.36 $m^2\ g^{-1}$, which is larger than that of N-PC@aCo (907.7 $m^2\ g^{-1}$) and N-PC (1014.1 $m^2\ g^{-1}$) hosts. The abundant micropore/mesopore structure of N-PC@uCo provides sufficient space to host S nanoparticles and the large surface area of N-PC@uCo efficiently ensures high contact interface between active materials and host. The improved BET surface area of N-PC@uCo is contributed by ZnCo-ZIF precursor, proper heating condition and the effect of glucose. First, BET surface area of ZnCo-ZIF is up to 1743.2 $m^2\ g^{-1}$ (Figure S3c, Supporting Information), which is higher than that of most reported ZIF and thus making it possible to obtain carbonated product with high BET surface area. Second, calcination conditions including heating rate, temperature, and time are also very critical. We used a low heating rate <2 °C min^{-1} to maintain the framework structure of ZIF, which was supported by the similar pore size (1–3 nm) of ZIF (Figure S3d, Supporting Information) before and (Figure 2b) after calcination. In addition, the evaporating of zinc is at $T > 800$ °C.[41] Keeping ZIF at 900 °C for 3 h allows the zinc to evaporate without acid leaching. Third, glucose is preferentially carbonized to stable carbon framework inside ZnCo-ZIF, which not only reduces the coordinated metal ions (Zn^{2+} and Co^{2+}) and promote metallic Zn evaporation,[42] but also is like an obstruction to prevent the aggregation of metallic Co at higher temperature. Therefore, we think that the proper heating condition and the effect of glucose make BET surface area of ZIF not go down too much after carbonization.

As shown in Figure 2c, the XRD patterns of three sulfur cathodes show characteristic peaks of sulfur and indicate that sulfur with high degree of crystallinity was composited with different cathode host successfully. As analyzed by TGA (Figure 2d), the content of sulfur in N-PC@uCo, PC@aCo, and N-PC are 76%, 66%, and 73%, respectively. Inset of Figure 2d shows that the start temperature of quality loss was different for three samples, and N-PC@uCo has a highest start temperature (≈200 °C) compared to other sulfur cathodes, suggesting that N-PC@uCo has a strong binding effect with sulfur. Furthermore, the electrical conductivities of three host structures before and after the sulfur loading were tested by using the four-point probe instrument. It can be seen from Figure 2e that the electrical conductivities of N-PC@uCo either before or after sulfur loading are higher than that of N-PC and N-PC@aCo. The improved electrical conductivity with the well-wrapped sulfur in N-PC@uCo

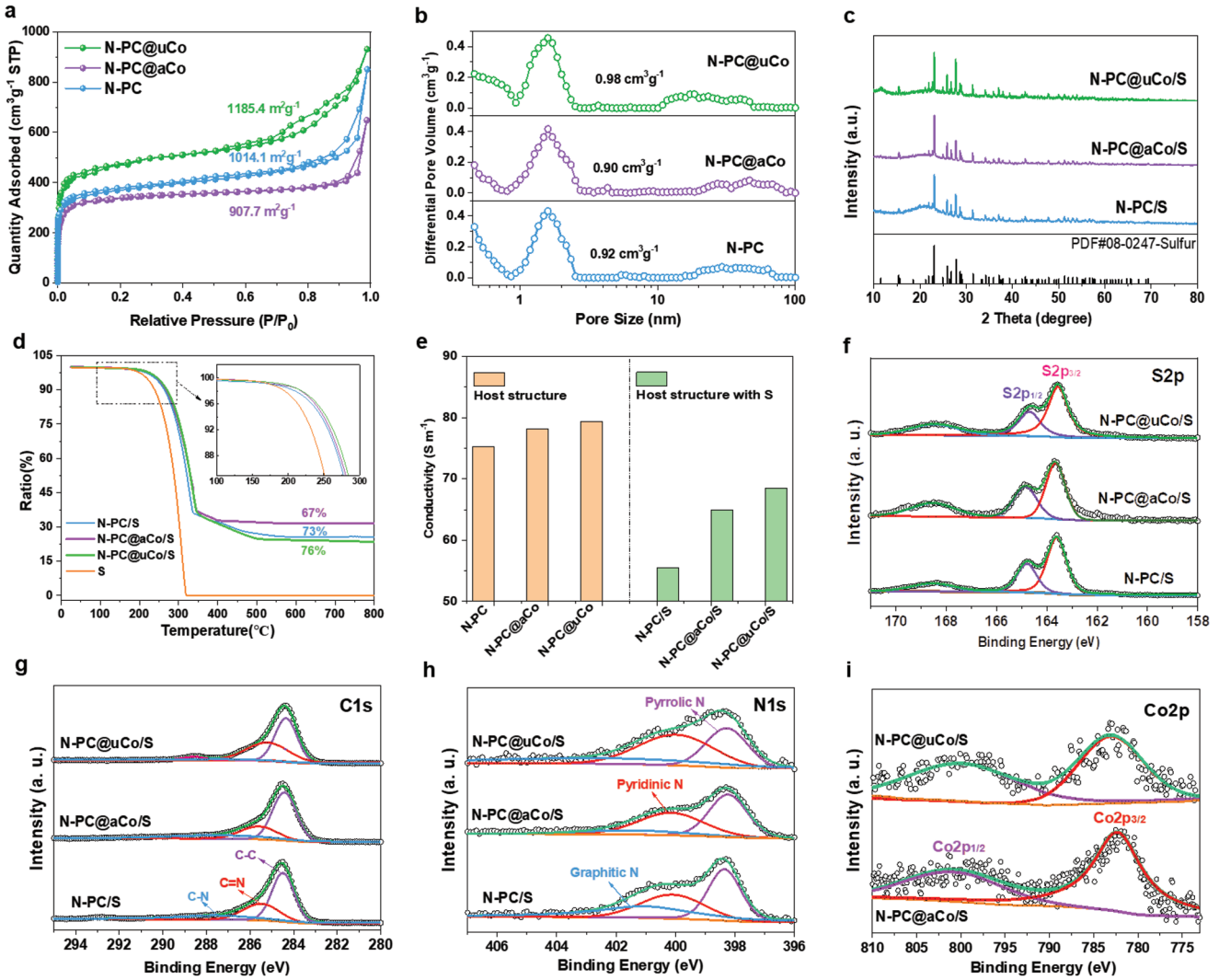

Figure 2. a) N_2 adsorption/desorption isotherms and b) pore size distribution of three host structures: N-PC, N-PC@aCo, and N-PC@uCo, c) XRD patterns, d) thermogravimetric analysis (TGA) patterns, e) conductivity, and binding energy of f) S 2p, g) C 1s, h) N 1s, and i) Co 2p in three sulfur cathodes: N-PC@uCo/S, N-PC@aCo/S, and N-PC/S.

should lead to significant depolarization in the electrode, and a facile electrochemical reaction kinetic is thus expected.

To investigate the existential form of C, N, S, Co elements in three sulfur cathodes, high-resolution X-ray photoelectron spectroscopy (XPS) measurements were carried out (Figure 2f–i). The binding energy of S2p[43,44] (Figure 2f) confirms the valence state of elemental sulfur. As shown in Figure 2g, the fitted C1s spectrum showed a main peak at around 284.8 eV, corresponding to sp^2 carbon, and peaks at 285.8 and 287.6 eV, assigned to C=N bonds and C—N species, respectively.[38] These results exactly confirmed the high conductivity of carbon framework and the formation of C—N bonds during the annealing process. The presence of nitrogen species in three sulfur cathodes were further revealed by the high-resolution N 1s spectrum (Figure 2h). Three characteristic peaks were located at 398.6, 400.8, and 401.3 eV, which corresponded to pyridinic, pyrrolic, and graphitic N species, respectively.[45,46] Figure 2i shows two characteristic peaks located at 780.3 and 795.9 eV in the high-resolution Co 2p spectrum, which are attributed to the metallic cobalt.[47,48] Previous reports illustrate that a N-doped carbon surface facilitates the oxidization of Li_2S_n (n = 3–8) by enhancing the adsorption energy and, consequently, improves the sulfur utilization and cyclic performance.[49–52]

To further demonstrate how the multifunctional cathode works, we compared the electrochemical performances of three cathodes (N-PC@uCo/S, N-PC@aCo/S, and N-PC/S) at 0.1C (1C = 1675 mA g^{-1}) over 100 cycles (**Figure 3**a). The initial discharge capacities of N-PC@uCo/S, N-PC@aCo/S, and N-PC/S reach 1380, 1214, and 1122 mAh g^{-1}, with corresponded columbic efficiency of 99.5%, 98.1%, and 96.4%, respectively. After 100 cycles, the capacity of N-PC@uCo/S, N-PC@aCo/S, and N-PC/S were 1150, 832, and 567 mAh g^{-1}, respectively. For further comparison, the rate performance of all the samples was evaluated at various current rates. The galvanostatic charge/discharge profiles of three cathodes at different rates of 0.1C, 0.2C, 0.5C, 1.0C, 2.0C, and 5.0C are depicted in Figure S13 in

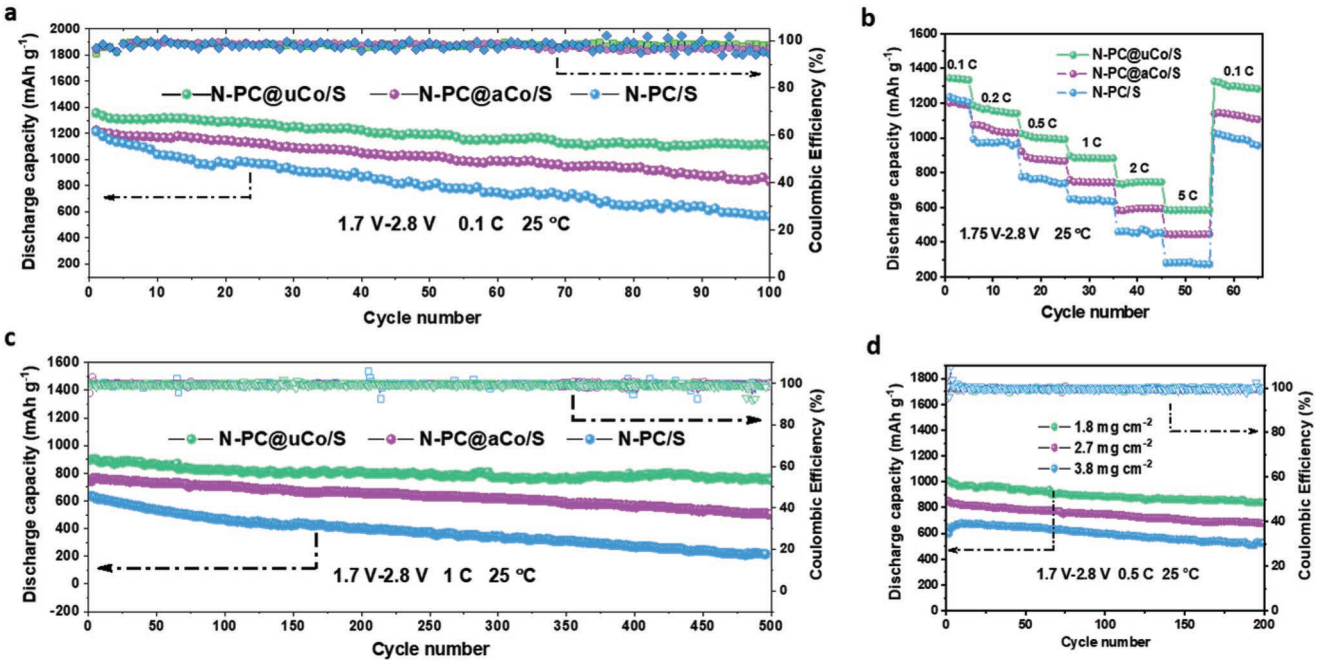

Figure 3. Electrochemical performance of N-PC@uCo/S, N-PC@aCo/S, and N-PC/S cathodes. a) Discharge capacity and columbic efficiency at 0.1C, b) rate capacity from 0.1C to 5C, c) cycling stability at 1C for 500 cycles with sulfur loading of 1.8 mg cm^{-2}, d) cycling capacity and columbic efficiency of N-PC@uCo/S with sulfur loading of 1.8, 2.7, and 3.8 mg cm^{-2}.

the Supporting Information. Compared with the N-PC@aCo/S and N-PC/S cathodes, the N-PC@uCo/S (Figure 3b) exhibited much higher capacity at the same discharge rates. When the current rates were increased from 0.1C to 0.2C, 0.5C, 1.0C, 2.0C, and 5.0C, the electrode exhibits reversible capacities from 1370 to 1180, 1102, 900, 740, and 600 mAh g^{-1}, respectively. As the current rate decreased back to 0.1C, the specific capacity of N-PC@uCo/S cathode recovered to 1320 mAh g^{-1}, indicating good stability and structural integrity of the electrode.

To evaluate the long-term cycling stability, the Li–S batteries based on N-PC@uCo/S cathodes were cycled at high current densities (Figure 3c). At the current rate of 1.0C, the N-PC@uCo/S cathode delivers an initial discharge capacity of 912 mAh g^{-1}. After 500 cycles, the specific capacity of N-PC@uCo/S is well maintained at 780 mAh g^{-1}, with a capacity retention of 86% and average columbic efficiency of 99.7%, which corresponds to a low capacity decay of only 0.028% per cycle. Compared with the N-PC@aCo/S and N-PC/S, the N-PC@uCo/S cathode exhibits much larger capacity at every cycles and higher retention within 500 cycles (Figure 3c). Considering that the high areal capacity is critical for practical application of Li–S batteries, the areal sulfur loading was increased from 1.8 to 2.7 and 3.8 mg cm^{-2} by fabricating thick electrodes. It can be observed (Figure 3d) that N-PC@uCo/S can maintain good discharge capacities of 850 and 675 mAh g^{-1} even at high sulfur loadings of 2.7 and 3.8 mg cm^{-2}. Even after 200 cycles, reversible capacities with 680 and 535 mAh g^{-1} still can be achieved, respectively. Furthermore, we tested the specific capacity of N-PC@uCo/S at a low rate of 0.2C with a high sulfur loading of 5.9 mg cm^{-2}. This cathode achieved a high current density of 4.8 mAh cm^{-2} and capacity retention of 91% for 100 cycles (Figure S14, Supporting Information). Under such high S utilization and areal capacity, it can be predicted that the cathode could achieve an energy density over 350 Wh kg^{-1} based on current liquid or solid battery technology.[53] Therefore, we conclude that the excellent electrochemical performances of N-PC@uCo/S cathode can be attributed to the special compositions and structures.

Next, we further explored the different effects of three host structures on the electrochemical behavior of sulfur cathode. **Figure 4**a shows the first charge/discharge curves of N-PC@uCo/S, N-PC@aCo/S, and N-PC/S between 1.7 and 2.7 V. For the discharge curves, ΔH_1 represents the capacity between 2.1 and 2.4 V which is provided by cathodic reduction process ($S_8 \rightarrow Li_2S_x$, $3 \le x \le 8$), ΔH_2 represents the capacity between 1.7 and 2.1 V provided by cathodic reduction process ($Li_2S_x \rightarrow Li_2S_2$/$Li_2S$). The detailed values of ΔH_1 and ΔH_2 were given in Figure S15 in the Supporting Information, the higher ΔH_1 means that more S_8 converts to lithium polysulfides, whereas longer platform in the range of ΔH_2 indicates that more Li_2S_x participates in reaction, less dissolution in electrolyte and faster reaction in the cathode. The results show that N-PC@uCo/S sample has more S_8 conversion and larger platform capacity which can be attributed to the uniform dispersed Co clusters enhance the adsorption and redox of polysulfide during discharging process.

To investigate the Li-ion diffusion kinetics in the three cathodes, the cyclic voltammetry (CV) at different scan rates from 0.1 to 0.4 mV s^{-1} were carried out (Figure 4b and Figure S16, Supporting Information). One major peak (I_A) can be observed in charge process and two peaks (I_B and I_C) in discharge process. I_A represents the anodic oxidation process and corresponds to $Li_2S_2/Li_2S \rightarrow S_8 + Li$. I_B between 2.1 and 2.4 V represents the cathodic reduction process of $S_8 \rightarrow Li_2S_x$ ($3 \le x \le 8$), and I_C between 1.7 and 2.1 V represents the cathodic reduction:

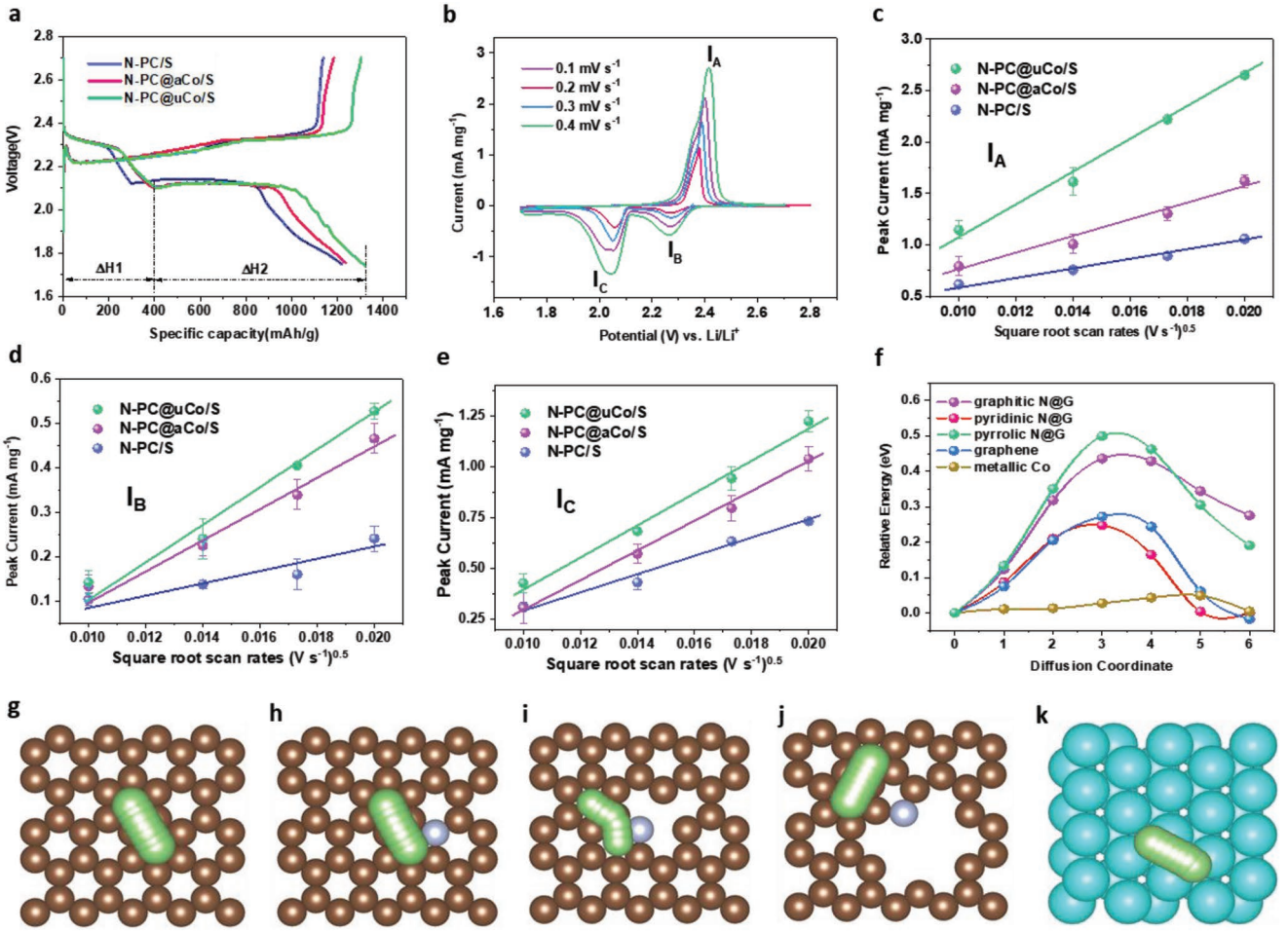

Figure 4. a) First charge/discharge voltage profiles of three sulfur cathodes with multiple effects, b) CV curves of N-PC@uCo/S at scan rates from 0.1 to 0.4 mV s^{-1}, c) CV curves peak current of I_A (anodic oxidation process, $Li_2S_2/Li_2S \rightarrow S_8+Li$), d) I_B (cathodic reduction process, $S_8 \rightarrow Li_2S_x$, $3 \le x \le 8$), e) I_C (cathodic reduction process, $Li_2S_x \rightarrow Li_2S_2/Li_2S$) for three cathodes with multiple effects, f) calculated energy barriers for Li-ion diffusion and the corresponding diffusion pathways for g) graphene, h) graphitic N@G, i) pyridinic N@G, j) pyrrolic N@G, and k) Co cluster, the green, gray, silvery, blue balls represent lithium, carbon, nitrogen atoms, respectively.

$Li_2S_x \rightarrow Li_2S_2/Li_2S$ ($3 \le x \le 8$). The lithium ion diffusion kinetics can be obtained according to the Randles–Sevcik equation[31,32]

$$I_P = \left(2.65 \times 10^5\right) n^{1.5} S D_{Li}^{0.5} C_{Li} v^{0.5} \quad (1)$$

where I_P is the peak current, n represents electron number, S represents electrode area, D_{Li} is the Li ion diffusion coefficient, C_{Li} is the Li ion concentration in the electrochemical reaction, v is the scan rate. As shown in Figure 4c–e, all the slopes of $I_P/v^{0.5}$ curves have positive correlation with D_{Li}. The detailed slope values of the curves ($I_P/v^{0.5}$) of I_A, I_B, I_C for three sulfur cathodes are fitted and calculated in Figure S17 in the Supporting Information. Compared to N-PC@aCo/S and N-PC/S, N-PC@uCo/S has an improved Li diffusion. Therefore, the results show that the highly dispersed Co clusters in N-PC@aCo/S can effectively accelerate the Li diffusion reaction.

To deeply understand why the uniform dispersed Co clusters can effectively accelerate the Li-ion diffusion kinetic process, we used density functional theory to calculate the barrier for Li diffusion on different samples (Figure 4f–k). The top views of Li diffusion path on graphene, graphitic N@G, pyridinic N@G, pyrrolic N@G, and Co cluster are shown in Figure 4g–k. Based on these paths, the energy barriers for Li ion transfer were 0.28, 0.42, 0.27, 0.49, and 0.05 eV, respectively (Figure 4f). We understand from the simulation results that N in the substrate can alter the diffusivity of Li ions to some extent, and that the lowest barrier energy (0.05 eV) for Li^+ transfer is obtained on Co cluster, which will most probably accelerate the kinetic reduction process: $Li_2S_x + Li^+ \rightarrow Li_2S_2/Li_2S$.

To probe the electrochemical conversion of polysulfides at the electrode/electrolyte interface, we assembled symmetric cells containing a 0.4 M Li_2S_6-DOL/DME solution as the electrolyte and N-PC, N-PC@aCo, or N-PC@uCo as the electrodes, and performed CV to oxidize and reduce the Li_2S_6 on the electrodes. Under identical measuring conditions, it is clearly observed that the N-PC@aCo and N-PC@uCo cells show higher CV current density (**Figure 5**a) together with lower charge transfer resistance than that of N-PC (Figure 5b), which demonstrates the Co cluster play a great role to accelerate redox conversion of polysulfides on the electrode surface. Furthermore, we used

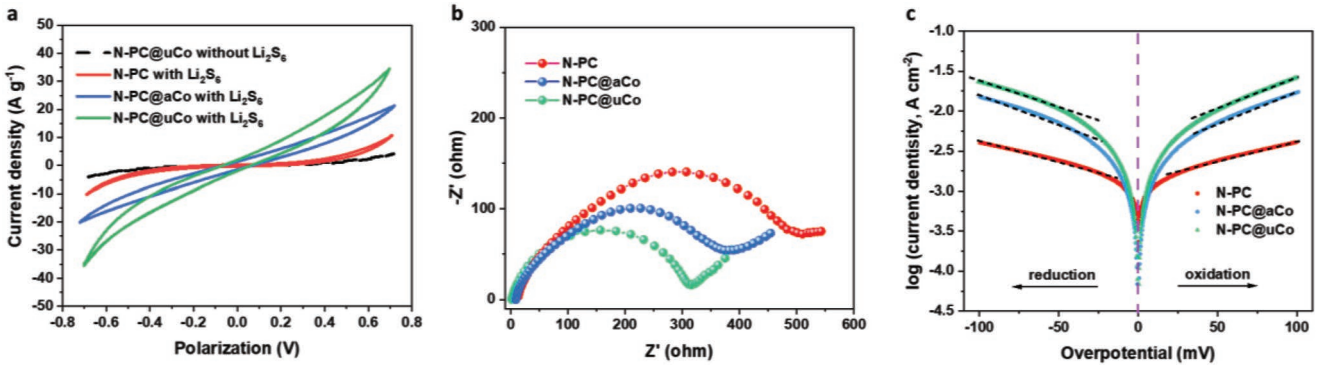

Figure 5. a) CVs at the scan rate of 10 mV s^{-1}, b) EIS spectra in the frequency range of 50 mHz–200 kHz, c) Tafel plots and exchange current densities of symmetric cells containing a 0.4 M Li_2S_6-DOL/DME solution as the electrolyte and N-PC, N-PC@aCo, or N-PC@uCo as the electrodes.

Tafel slope and exchange current density to quantify the catalytic activity of each sample in polysulfide formations. Tafal plots of the three electrodes, derived from CV experiments, are displayed in Figure 5c. Based on the following formula[54,55]

$$\eta = a + b \lg I \tag{2}$$

where, η is the overpotential, I is the current density. The calculated exchange current densities of N-PC, N-PC@aCo, or N-PC@uCo were 1.43, 3.56, and 4.52 mA cm^{-2} for the cathodic process and 1.40, 3.08, and 4.17 mA cm^{-2} for anodic process. The higher exchange current density value of N-PC@uCo relative to that of N-PC and N-PC@aCo confirms the enhancement in rate of polysulfides conversion reactions. Therefore, we conclude that the highly dispersed Co clusters as catalyst in N-PC@aCo/S can effectively accelerate the reduction of polysulfides.

To further study the absorption effect between Li_2S_x (x = 4, 6, 8) and samples, the first-principle simulations were performed. As shown in **Figure 6**a, graphene, graphitic N@G, pyridinic N@G, pyrrolic N@G, and Co cluster were selected as the representative to calculate the binding energy with Li_2S_x (x = 4, 6, 8). From the top view of adsorption conformations of Li_2S_x (x = 4, 6, 8) and graphene, graphitic N@G, pyridinic N@G, pyrrolic N@G and Co cluster, we can conclude that the chemical interaction is the most important interaction between the Li ion in Li_2S_x (x = 4, 6, 8) and graphene, graphitic N@G, pyridinic N@G, pyrrolic N@G, and Co cluster. The binding energy can be calculated according to references.[35,56,57] The binding strengths between Li_2S_x (x = 4, 6, 8) and graphene, graphitic N@G, pyridinic N@G, pyrrolic N@G, and Co cluster are shown in Figure 6b, and it is found that the Co cluster has the highest binding energy for Li_2S_x (x = 4, 6, 8) as compared to graphene, graphitic N@G, pyridinic N@G, pyrrolic N@G.

Next, polysulfide adsorption experiments (Figure 6c), XPS results (Figure 6d,e), and in situ beaker cell observation experiments (Figure 6f) were used to verify the strong absorption effect of highly dispersed Co cluster on polysulfide. As shown in Figure 6c, after adding of N-PC@uCo and N-PC@aCo, both colors of Li_2S_6 solution immediately become colorless, while for N-PC, the Li_2S_6 solution just turns lighter. This indicates the stronger adsorption ability of Co cluster with sulfur species is consistent with the theoretical simulation. XPS data were collected on the N-PC@uCo solid with Li_2S_6. As illustrated in Figure 6d, the S 2p spectrum of N-PC@uCo-Li_2S_6 shows four peaks. Two peaks situated at 161.8 and 162.8 eV, respectively, are assigned to the terminal (S_T^{-1}) and bridging (S_B^0) S atoms in Li_2S_6, the positive shift (≈0.5 eV) of S_T^{-1} and bridging S_B^0 peaks in N-PC@uCo-Li_2S_6 confirms electron transfer between N-PC@uCo host and electronegative polysulfide.[44,58] While another two peaks at 166.8 and 167.9 eV are attributed to the binding energy of polythionate and thiosulfate complex, which are caused by the polysulfide redox reaction with N-PC@uCo.[59,60] the Co—S bond in Co 2p (Figure 6e) further confirms the chemisorption of Li_2S_6 on the surface of Co cluster. In addition, we used in situ beaker cell observation experiments to contrast the polysulfide dissolved in electrolyte of N-PC/S, N-PC@aCo/S, and N-PC@uCo/S (Figure 6f). It can be clearly observed that at the initial moment, the color of the electrolyte for all cells was clear and transparent. However, after discharged for 15 h at 0.025C (1C in Figure S18, Supporting Information) many yellow materials were in electrolyte for N-PC/S which corresponded to polysulfide dissolution. Different from the N-PC/S, less polysulfides appeared in electrolyte for N-PC@aCo/S. More importantly, the electrolyte for N-PC@uCo/S cell was still clear and transparent, demonstrating almost no polysulfide appeared during cycling. These results demonstrate that high dispersion of Co cluster in sample can make Co cluster trap more lithium polysulfides and then accelerate the redox during cycling which plays a great role in enhancing the stability of Li–S battery.

Comparing with other reported MOF derived electrode materials with high loading sulfur (Table S1, Supporting Information), the new sulfur cathode we designed exceeds the most reported materials in cycle life and high rate capacity, which can be attributed to the advantages of the host structure obtained by introducing glucose during ZnCo-ZIF carbonization. First, N-PC@uCo host has high BET surface area (1185.36 m^2 g^{-1}) with large pore volume (V = 0.98 cm^3 g^{-1}), which are larger than that of common annealed MOF (300–500 m^2 g^{-1}).[35,37,44] Combined with the density of sulfur (ρ = 1.96 g cm^{-3}),[61] the sulfur loading within carbon cage was calculated by the following formula

$$\text{Sulfur loading}\,(\%) = \frac{V \times \rho}{1 + V \times \rho} = \frac{0.98 \times 1.96}{1 + 0.98 \times 1.96} = 66\% \tag{3}$$

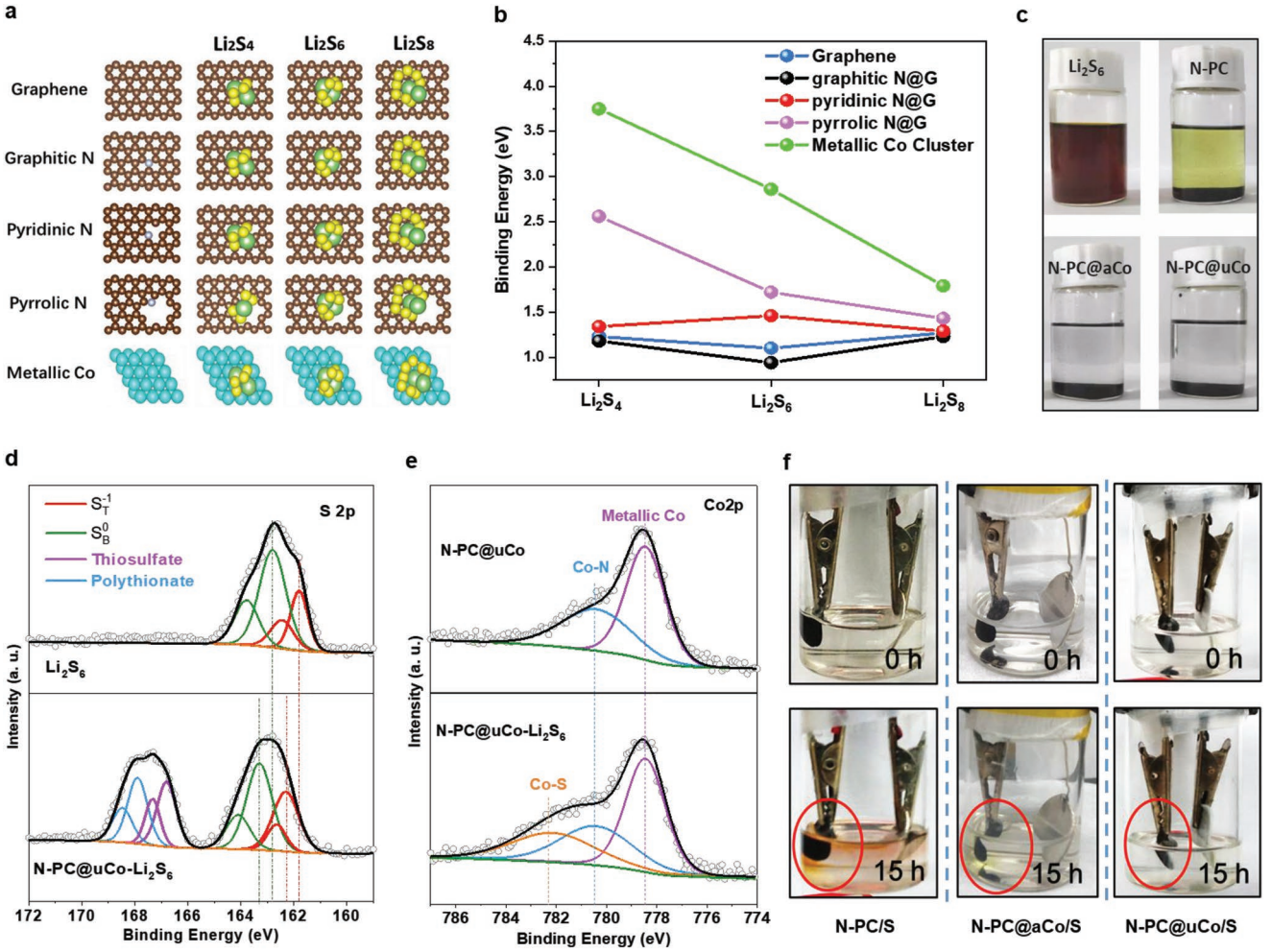

Figure 6. a) Atomic conformations and b) calculated binding energy for Li_2S_4, Li_2S_6, Li_2S_8 species adsorption on graphene, graphitic N@G, pyridinic N@G, pyrrolic N@G, Co particle, the green, gray, silvery, blue balls represent lithium, carbon, nitrogen atoms, respectively, c) polysulfide adsorption experiments, d,e) XPS at the binding energy of S 2p and Co 2p, f) in situ beaker cell observation experiments to contrast the polysulfide dissolved in electrolyte of N-PC/S, N-PC@aCo/S, and N-PC@uCo/S.

The internal sulfur is in close contact with the carbon framework and hard to dissolve in electrolyte relative to sulfur on the outside, thus high ratio of internal sulfur (87% = 66%/76%) leads to very high reversibility during cycling. In addition, glucose itself converted into sp^2 carbon to improve the electrical conductivity of host, thus leading to significant depolarization in the sulfur cathode. More importantly, the adding of glucose enhances dispersion of the Co catalyst in carbon cage, which promotes a high coverage of polysulfide on the surface of catalyst, thus, the adsorption and conversion of polysulfide are more efficient.

3. Conclusion

In summary, we have designed a porous carbon nanocage with nitrogen doping and uniform dispersed cobalt catalyst as a host structure for sulfur. The uniformity and size of Co cluster can be effectively controlled in the synthesis process by adding glucose. We found that the fabricated host structure possesses multiple effects acting as sulfur host, such as high conductivity, high sulfur loading, effective stress relief, as well as good contact in the interface between active materials and sulfur host. Highly dispersed Co cluster in sulfur cathodes can not only accelerate the lithium-ion diffusion and redox of polysulfide, but also enhance the absorption of polysulfides. Our work provides Li/polysulfide kinetics and adsorption benchmarks for future DFT calculations in Li–S batteries and highlights an opportunity to exploit transition metal clusters as polysulfide catalysts for designing high-performance Li–S batteries.

Supporting Information

Supporting Information is available from the Wiley Online Library or from the author.

Acknowledgements

The research was financially supported by National Natural Science Foundation of China (51602009), International Postdoctoral Exchange

Fellowship Program (20170098), China Postdoctoral Science Foundation (2016M600008), National Key R&D Program of China (2016YFB0700600), Soft Science Research Project of Guangdong Province (No. 2017B030301013), and Shenzhen Science and Technology Research Grant (ZDSYS201707281026184).

Conflict of Interest

The authors declare no conflict of interest.

Author Contributions

R.W. and J.Y. contributed equally to this work. R.W. and J.Y. designed the project and performed the preparation of materials. R.W., J.Y., W.Z., Y.Y., and G.Z. carried out measurements and data analyses. X.C. performed the DFT calculations. J.Y., G.Q., Y.X., Y.Y., G.Z., and F.P. discussed the results, analyzed the data, and drafted the manuscript. All authors reviewed the manuscript.

Keywords

cobalt clusters, density functional theory calculations, Li–S batteries, porous carbon, sulfur host

Received: October 30, 2019
Revised: December 8, 2019
Published online: January 31, 2020

[1] A. Rosenman, E. Markevich, G. Salitra, D. Aurbach, A. Garsuch, F. F. Chesneau, *Adv. Energy Mater.* **2015**, *5*, 1500212.
[2] J. Lu, Z. Chen, F. Pan, Y. Cui, K. Amine, *Electrochem. Energy Rev.* **2018**, *1*, 35.
[3] Z. W. Seh, Y. Sun, Q. Zhang, Y. Cui, *Chem. Soc. Rev.* **2016**, *45*, 5605.
[4] A. Manthiram, Y. Fu, S. H. Chung, C. Zu, Y. S. Su, *Chem. Rev.* **2014**, *114*, 11751.
[5] A. Manthiram, S. H. Chung, C. Zu, *Adv. Mater.* **2015**, *27*, 1980.
[6] X. Zhang, A. Chen, M. Zhong, Z. Zhang, X. Zhang, Z. Zhou, X. Bu, *Electrochem. Energy Rev.* **2019**, *2*, 29.
[7] H. Peng, J. Huang, X. Cheng, Q. Zhang, *Adv. Energy Mater.* **2017**, *7*, 54.
[8] R. Fang, S. Zhao, Z. Sun, D. W. Wang, H. M. Cheng, F. Li, *Adv. Mater.* **2017**, *29*, 1606823.
[9] J. Guo, Y. Xu, C. Wang, *Nano Lett.* **2011**, *11*, 4288.
[10] S. H. Chung, A. Manthiram, *Electrochim. Acta* **2013**, *107*, 569.
[11] S. H. Chung, A. Manthiram, *Adv. Mater.* **2014**, *26*, 1360.
[12] J. S. Lee, W. Kim, J. Jang, A. Manthiram, *Adv. Energy Mater.* **2017**, *7*, 1601943.
[13] L. Miao, W. Wang, K. Yuan, Y. Yang, A. Wang, *Chem. Commun.* **2014**, *50*, 13231.
[14] X. Ji, K. T. Lee, L. F. Nazar, *Nat. Mater.* **2009**, *8*, 500.
[15] Z. Sun, M. Xiao, S. Wang, D. Han, S. Song, G. Chen, Y. Meng, *J. Power Sources* **2015**, *285*, 478.
[16] Z. Li, Y. Jiang, L. Yuan, Z. Yi, C. Wu, Y. Liu, P. Strasser, Y. Huang, *ACS Nano* **2014**, *8*, 9295.
[17] Y. Mao, G. Li, Y. Guo, Z. Li, C. Liang, X. Peng, Z. Lin, *Nat. Commun.* **2017**, *8*, 14628.
[18] H. Kim, H. D. Lim, J. Kim, K. Kang, *J. Mater. Chem. A* **2013**, *2*, 33.
[19] L. Sun, M. Li, Y. Jiang, W. Kong, K. Jiang, J. Wang, S. Fan, *Nano Lett.* **2014**, *14*, 4044.
[20] N. Jayaprakash, J. Shen, S. S. Moganty, A. Corona, L. A. Archer, *Angew. Chem., Int. Ed.* **2011**, *50*, 5904.
[21] Y. Zhang, Z. Bakenov, Y. Zhao, A. Konarov, T. N. L. Doan, M. Malik, T. Paron, P. Chen, *J. Power Sources* **2012**, *208*, 1.
[22] Z. Li, C. Li, X. Ge, J. Ma, Z. Zhang, Q. Li, C. Wang, L. Yin, *Nano Energy* **2016**, *23*, 15.
[23] L. Wang, J. Liu, S. Yuan, Y. Wang, Y. Xia, *Energy Environ. Sci.* **2016**, *9*, 224.
[24] Y. Yang, Y. Zhong, Q. Shi, Z. Wang, K. Sun, H. Wang, *Angew. Chem., Int. Ed.* **2018**, *57*, 15549.
[25] L. Li, L. Chen, S. Mukherjee, J. Gao, H. Sun, Z. B. Liu, X. L. Ma, T. Gupta, C. V. Singh, W. C. Ren, H. M. Cheng, N. Koratkar, *Adv. Mater.* **2017**, *29*, 8.
[26] J. S. Lee, J. Jun, J. Jang, A. Manthiram, *Small* **2017**, *13*, 1602984.
[27] S. H. Li, X. H. Xia, Y. D. Wang, X. L. Wang, J. P. Tu, *J. Power Sources* **2017**, *342*, 224.
[28] J. S. Lee, A. Manthiram, *J. Power Sources* **2017**, *343*, 54.
[29] X. Liang, C. Y. Kwok, F. Lodi-Marzano, Q. Pang, M. Cuisinier, H. Huang, C. J. Hart, D. Houtarde, K. Kaup, H. Sommer, T. Brezesinski, J. Janek, L. F. Nazar, *Adv. Energy Mater.* **2016**, *6*, 9.
[30] C. Zheng, S. Niu, W. Lv, G. Zhou, J. Li, S. Fan, Y. Deng, Z. Pan, B. Li, F. Kang, Q. H. Yang, *Nano Energy* **2017**, *33*, 306.
[31] J. Xu, W. Zhang, H. Fan, F. Cheng, D. Su, G. Wang, *Nano Energy* **2018**, *51*, 73.
[32] G. Zhou, H. Tian, Y. Jin, X. Tao, B. Liu, R. Zhang, Z. W. Seh, D. Zhuo, Y. Liu, J. Sun, J. Zhao, C. Zu, D. S. Wu, Q. Zhang, Y. Cui, *Proc. Natl. Acad. Sci. USA* **2017**, *114*, 840.
[33] Z. Yuan, H. J. Peng, T. Z. Hou, J. Q. Huang, C. M. Chen, D. W. Wang, X. B. Cheng, F. Wei, Q. Zhang, *Nano Lett.* **2016**, *16*, 519.
[34] L. Ma, S. Wei, H. L. Zhuang, K. E. Hendrickson, R. G. Hennig, L. A. Archer, *J. Mater. Chem. A* **2015**, *3*, 19857.
[35] T. G. Jeong, D. S. Choi, H. Song, J. Choi, S. A. Park, S. H. Oh, H. Kim, Y. Jung, Y. T. Kim, *ACS Energy Lett.* **2017**, *2*, 327.
[36] Z. Wang, J. Shen, J. Liu, X. Xu, Z. Liu, R. Hu, L. Yang, Y. Feng, Z. Shi, L. Ouyang, Y. Yu, M. Zhu, *Adv. Mater.* **2019**, *31*, 1902228.
[37] J. Zhou, R. Li, X. Fan, Y. Chen, R. Han, W. Li, J. Zheng, B. Wang, X. Li, *Energy Environ. Sci.* **2014**, *7*, 2715.
[38] Y. J. Li, J. M. Fan, M. S. Zheng, Q. F. Dong, *Energy Environ. Sci.* **2016**, *9*, 1998.
[39] M. Yang, X. Hu, Z. Fang, L. Sun, Z. Yuan, S. Wang, W. Hong, X. Chen, D. Yu, *Adv. Funct. Mater.* **2017**, *27*, 1701971.
[40] T. Chen, B. Cheng, G. Zhu, R. Chen, Y. Hu, L. Ma, H. Lv, Y. Wang, J. Liang, Z. Tie, Z. Jin, J. Liu, *Nano Lett.* **2017**, *17*, 437.
[41] E. Fletcher, *Ind. Eng. Chem. Res.* **1999**, *38*, 2275.
[42] P. Zhang, F. Sun, Z. Xiang, Z. Shen, J. Yun, D. Cao, *Energy Environ. Sci.* **2014**, *7*, 442.
[43] Z. Wang, Y. Dong, H. Li, Z. Zhao, H. B. Wu, C. Hao, S. Liu, J. Qiu, X. W. Lou, *Nat. Commun.* **2014**, *5*, 5002.
[44] R. Wang, K. Wang, S. Gao, M. Jiang, J. Han, M. Zhou, S. Cheng, K. Jiang, *Nanoscale* **2018**, *10*, 16730.
[45] X. Wang, J. Zhou, H. Fu, W. Li, X. Fan, G. Xin, J. Zheng, X. Li, *J. Mater. Chem. A* **2014**, *2*, 14064.
[46] L. Zhang, Z. Su, F. Jiang, L. Yang, J. Qian, Y. Zhou, W. Li, M. Hong, *Nanoscale* **2014**, *6*, 6590.
[47] J. He, Y. Chen, W. Lv, K. Wen, C. Xu, W. Zhang, Y. Li, W. Qin, W. He, *ACS Nano* **2016**, *10*, 10981.
[48] M. Zhong, J. Guan, Q. Feng, X. Wu, Z. Xiao, W. Zhang, S. Tong, N. Zhou, D. Gong, *Carbon* **2018**, *128*, 86.
[49] Y. Liu, G. Li, Z. Chen, X. Peng, *J. Mater. Chem. A* **2017**, *5*, 9775.
[50] J. Zhang, M. Huang, B. Xi, K. Mi, A. Yuan, S. Xiong, *Adv. Energy Mater.* **2018**, *8*, 1701330.
[51] L. C. Yin, J. Liang, G. M. Zhou, F. Li, R. Saito, H. M. Cheng, *Nano Energy* **2016**, *25*, 203.
[52] F. Pei, T. An, J. Zang, X. Zhao, X. Fang, M. Zheng, Q. Dong, N. Zheng, *Adv. Energy Mater.* **2016**, *6*, 1502539.

[53] C. Li, H. Zhang, L. Otaegui, G. Singh, M. Armand, L. Rodriguez-Martinez, *J. Power Sources* **2016**, *326*, 1.
[54] Q. Pang, C. Kwok, D. Kundu, X. Liang, L. F. Nazar, *Joule* **2019**, *3*, 136.
[55] Y. Wang, R. Zhang, Y. Pang, X. Chen, J. Lang, J. Xu, C. Xiao, H. Li, K. Xi, S. Ding, *Energy Storage Mater.* **2019**, *16*, 228.
[56] G. Zhou, K. Liu, Y. Fan, M. Yuan, B. Liu, W. Liu, F. Shi, Y. Liu, W. Chen, J. Lopez, D. Zhuo, J. Zhao, Y. Tsao, X. Huang, Q. Zhang, Y. Cui, *ACS Cent. Sci.* **2018**, *4*, 260.
[57] Q. Zhang, Y. Wang, Z. W. Seh, Z. Fu, R. Zhang, Y. Cui, *Nano Lett.* **2015**, *15*, 3780.
[58] M. Chen, W. Xu, S. Jamil, S. Jiang, C. Huang, X. Wang, Y. Wang, H. Shu, K. Xiang, P. Zeng, *Small* **2018**, *14*, 1803134.
[59] X. Liang, C. Hart, Q. Pang, A. Garsuch, T. Weiss, L. F. Nazar, *Nat. Commun.* **2015**, *6*, 5682.
[60] X. Wang, C. Yang, X. Xiong, G. Chen, M. Huang, J. Wang, Y. Lui, M. Liu, K. Huang, *Energy Storage Mater.* **2019**, *16*, 344.
[61] D. Sands, *J. Am. Chem. Soc.* **1965**, *87*, 1395.

